The Astrophysical Journal, 846:9 (9pp), 2017 September 1 https://doi.org/10.3847/1538-4357/aa83b9
© 2017. The American Astronomical Society. All rights reserved.

# Spectroscopic Inversions of the Ca II 8542 Å Line in a C-class Solar Flare

D. Kuridze[1,5], V. Henriques[1,2], M. Mathioudakis[1], J. Koza[3], T. V. Zaqarashvili[4,5,6], J. Rybák[3], A. Hanslmeier[4], and F. P. Keenan[1]
[1] Astrophysics Research Centre, School of Mathematics and Physics, Queen's University Belfast, Belfast BT7 1NN, UK; d.kuridze@qub.ac.uk
[2] Institute of Theoretical Astrophysics, University of Oslo, P.O. Box 1029 Blindern, NO-0315 Oslo, Norway
[3] Astronomical Institute, Slovak Academy of Sciences, 059 60 Tatranska Lomnica, Slovakia
[4] IGAM, Institute of Physics, University of Graz, Universitätsplatz 5, A-8010 Graz, Austria
[5] Abastumani Astrophysical Observatory at Ilia State University, 3/5 Cholokashvili Avenue, 0162 Tbilisi, Georgia
[6] Space Research Institute, Austrian Academy of Sciences, Schmiedlstrasse 6, A-8042 Graz, Austria
*Received 2017 May 24; revised 2017 July 28; accepted 2017 July 31; published 2017 August 28*

## Abstract

We study the C8.4-class solar flare SOL2016-05-14T11:34 UT using high-resolution spectral imaging in the Ca II 8542 Å line obtained with the CRISP imaging spectropolarimeter on the Swedish 1 m Solar Telescope. Spectroscopic inversions of the Ca II 8542 Å line using the non-LTE code NICOLE are used to investigate the evolution of the temperature and velocity structure in the flaring chromosphere. A comparison of the temperature stratification in flaring and non-flaring areas reveals strong footpoint heating during the flare peak in the lower atmosphere. The temperature of the flaring footpoints between $\log \tau_{500} \approx -2.5$ and $-3.5$, where $\tau_{500}$ is the continuum optical depth at 500 nm, is ~5–6.5 kK close to the flare peak, reducing gradually to ~5 kK. The temperature in the middle and upper chromosphere, between $\log \tau_{500} \approx -3.5$ and $-5.5$, is estimated to be ~6.5–20 kK, decreasing to preflare temperatures, ~5–10 kK, after approximately 15 minutes. However, the temperature stratification of the non-flaring areas is unchanged. The inverted velocity fields show that the flaring chromosphere is dominated by weak downflowing condensations at the formation height of Ca II 8542 Å.

*Key words:* radiative transfer – Sun: atmosphere – Sun: chromosphere – Sun: flares – Sun: photosphere – techniques: imaging spectroscopy

## 1. Introduction

It is now widely accepted that the chromosphere is a key to our understanding of solar flares, because of the large amount of radiative loss that originates in it (Fletcher et al. 2011). Chromospheric radiation can provide vital diagnostics for the structure and dynamics of plasma parameters, such as temperature, velocity, density, pressure, and magnetic field in the flaring atmosphere.

The method of choice for studies of the one-dimensional vertical stratification of solar and stellar atmospheres has been the use of semi-empirical models that attempt to reproduce the observed profiles in LTE or non-LTE radiative transfer (e.g., see the review by Mauas 2007). Such an approach has been successful for the quiet-Sun (QS) atmosphere, for which static 1D models, developed under an assumption of hydrostatic equilibrium, reproduce chromospheric spectral lines and continua (Gingerich et al. 1971; Vernazza et al. 1981; Fontenla et al. 1990, 1991, 1993, 2006, 2009; Rutten & Uitenbroek 2012).

The first set of static semi-empirical models of a flaring photosphere and chromosphere was developed by Machado & Linsky (1975). These authors modeled the wings of the Ca II H&K lines and concluded that the region of minimum temperature in flares is both hotter and formed deeper in the atmosphere than in the QS models. Machado et al. (1980) developed models for a bright flare and a faint one that reproduce lines and continua of H I, Si I, C I, Ca II, and Mg II, and show a substantial temperature enhancement from the photosphere up to the transition region. Semi-empirical models of a white-light flare also show that flare-related perturbations can affect the formation heights of the wings and continuum, as well as the continuum emission originating in the photosphere (Mauas 1990, 1993; Mauas et al. 1990).

Gan & Fang (1987) and Gan et al. (1993) used H$\alpha$ line profiles to construct semi-empirical models for two flares that showed evidence for chromospheric condensations, which can reproduce the well-observed asymmetries in H$\alpha$ line profiles in flares. Moreover, Gan & Mauas (1994) found that condensations can increase the back-warming of the atmosphere, leading to heating of the photosphere and enhancement of the continuum emission. The evolution of chromospheric velocity fields during solar flares was also studied by Falchi & Mauas (2002) and Berlicki et al. (2005). Falchi & Mauas (2002) constructed five semi-empirical models for different flare evolution times, which reproduce the profiles of the H$\delta$, Ca II K, and Si I 3905 Å lines. Velocity fields were included to reproduce the asymmetric line profiles. Berlicki et al. (2008) performed semi-empirical modeling of the solar flaring atmosphere above sunspots using NLTE radiative transfer techniques. They found that the flaring layers (loops) are dominated by chromospheric evaporation, leading to a significant increase in gas pressure. Flare models obtained with forward radiative hydrodynamic codes such as RADYN (Carlsson & Stein 1997) can also reproduce the observed asymmetric line profiles and increase in temperature in the lower solar atmosphere (Kuridze et al. 2015, 2016).

A powerful way to construct atmospheric models with a semi-empirical approach is to fit the observed Stokes profiles using inversion algorithms (de la Cruz Rodríguez & van Noort 2016). Through such inversions, the ionization equilibrium, statistical equilibrium, and radiative transfer equations are solved numerically to synthesize the Stokes profiles under a set of predefined initial atmospheric conditions. Differences between the observed and synthetic profiles are used to modify, at a height usually determined by a response function, an initial model atmosphere that is used to reproduce the observed spectral signatures.

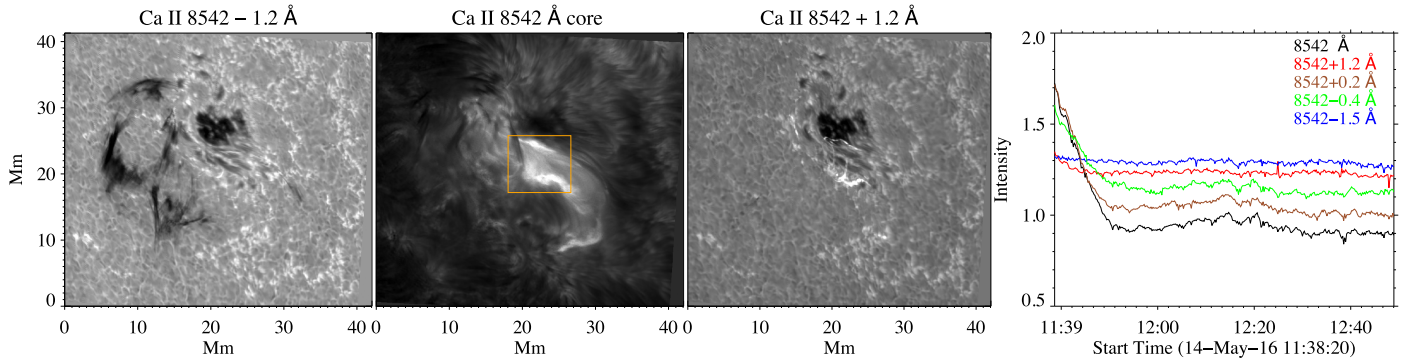


**Figure 1.** Images in the Ca II 8542 Å line wing and core obtained with the CRISP instrument on the SST at 11:38:20 UT on 2016 May 14. The orange box indicates the flaring region analyzed in this paper. The temporal evolution of the region averaged over the area marked with the yellow box is presented in the far right panel.

Several inversions have been performed in the Ca II H line using the LTE Stokes Inversion based on Response functions code (SIR, Ruiz Cobo & del Toro Iniesta 1992). A first-order NLTE correction was applied to obtain the temperature stratification of the chromosphere of the QS and active region (Beck et al. 2013, 2015). However, the development of NLTE radiative transfer codes, such as HAZEL (Asensio Ramos et al. 2008), HELIX$^+$ (Lagg et al. 2009), and NICOLE (Socas-Navarro et al. 2015), combined with the increased computational power available, also make NLTE inversions possible (see the review by de la Cruz Rodríguez & van Noort 2016).

The Ca II infrared (IR) triplet line at 8542 Å is well suited for the development of chromospheric models, due to its sensitivity to physical parameters, including magnetic field, in the solar photosphere and chromosphere (Pietarila et al. 2007; Cauzzi et al. 2008; Quintero Noda et al. 2016). Furthermore, the optimization of NICOLE for Ca II 8542 Å allows the use of this feature for the computation of semi-empirical atmospheric models. For more details about the spectropolarimetric capabilities of Ca II 8542 Å the reader is referred to Quintero Noda et al. (2016).

Inversions with NICOLE have been successfully performed for spectropolarimetric Ca II 8542 Å observations of umbral flashes in sunspots (de la Cruz Rodríguez et al. 2013), and granular-sized magnetic elements (magnetic bubbles) in an active region (de la Cruz Rodríguez et al. 2015a). In this paper we use NICOLE to invert high-resolution Ca II 8542 Å spectral imaging observations to construct models for the lower atmosphere of a solar flare. Multiple inversions were performed for the observed region covering flare ribbons and for non-flaring areas at different times during the event. From the constructed models we investigate the structural, spatial, and temporal evolutions of basic physical parameters in the upper photosphere and chromosphere during the flare.

## 2. Observations and Data Reduction

The observations were undertaken between 11:38 and 12:49 UT on 2016 May 14 close to the west limb (877″, −66″), near the equator at $\mu = 0.54$ with the CRisp Imaging Spectro-Polarimeter (CRISP; Scharmer 2006; Scharmer et al. 2008) instrument, mounted on the Swedish 1 m Solar Telescope (SST; Scharmer et al. 2003a) on La Palma. Adaptive optics were used throughout the observations, consisting of a tip–tilt mirror and an 85-electrode deformable mirror setup that is an upgrade of the system described in Scharmer et al. (2003b). The observations comprised spectral imaging in the H$\alpha$ 6563 Å and Ca II 8542 Å lines. All data were reconstructed with multi-object, multi-frame blind deconvolution (MOMFBD; van Noort et al. 2005). The CRISP instrument includes three different cameras. One camera acquires wideband (WB) images directly from the prefilter, and two narrowband (NB) cameras placed after a 50/50 polarizing beam splitter acquire narrowband (transmitted and reflected) components of horizontal and vertical polarization, each combination of camera, wavelength, and component being an object for reconstruction (for setup details, see, e.g., de la Cruz Rodríguez et al. 2015b). The WB channel provides frames for every time step, synchronously with the other cameras, and can be used as an alignment reference. The images, reconstructed from the narrowband wavelengths, are aligned at the smallest scales by using the method described by Henriques (2013). This employs cross-correlation between auxiliary wideband channels, obtained from an extended MOMFBD scheme, to account for different residual small-scale seeing distortions. We applied the CRISP data reduction pipeline as described in de la Cruz Rodríguez et al. (2015b), which includes small-scale seeing compensation as in Henriques (2012). Our spatial sampling was 0.″057 pixel$^{-1}$ and the spatial resolution was close to the diffraction limit of the telescope for many images in the time series over the 41 × 41 Mm$^2$ field of view. For the H$\alpha$ line scan we observed in 15 positions symmetrically sampled from the line core in 0.2 Å steps. The Ca II 8542 Å scan consisted of 25 line positions ranging from −1.2 Å to +1.2 Å from the line core in 0.1 Å steps, plus one position at −1.5 Å. A full spectral scan for both lines had a total acquisition time of 12 s, which is the temporal cadence of the time series. However, we note that the present paper includes only the analysis of the Ca II 8542 Å data, which had a duration of 7 s per scan. The transmission FWHM for Ca II 8542 Å is 107.3 mÅ with a prefilter FWHM of 9.3 Å (de la Cruz Rodríguez et al. 2015b). A two-ribbon C8.4 flare was observed in active region NOAA 12543 during our observations. Throughout the analysis we made use of CRISPEX (Vissers & Rouppe van der Voort 2012), a versatile widget-based tool for effective viewing and exploration of multi-dimensional imaging spectroscopy data.

Figure 1 shows a sample of the flare images in the Ca II 8542 Å line core and wing positions. Our observations commenced 4 minutes after the main flare peak (∼11:34 UT). Light curves generated from the region marked with the orange box in Figure 1 show the post-peak evolution of the emission in the line core and wings (right panel of Figure 1). Although we missed the rise phase and flare peak, two bright ribbons associated with post-flare emission are clearly detected at 11:38 UT with good spatial and temporal coverage.

## 3. Inversions

We used the NICOLE inversion algorithm (Socas-Navarro et al. 2015), which has been parallelized to solve multi-level, NLTE radiative transfer problems (Socas-Navarro & Trujillo Bueno 1997). This code iteratively perturbs physical parameters such as temperature, line-of-sight (LOS) velocity, magnetic field, and microturbulence of an initial guess model atmosphere to find the best match with the observations (Socas-Navarro et al. 2000). The output stratifications of the electron and gas pressures, as well as the densities, are computed from the equation of state using the temperature stratification and the upper boundary condition for the electron pressure under the assumption of hydrostatic equilibrium.

NICOLE includes a Ca II model atom consisting of five bound levels plus continuum (Leenaarts et al. 2009) with complete frequency redistribution, which is applicable for lines such as Ca II 8542 Å (Uitenbroek 1989; Wedemeyer-Böhm & Carlsson 2011; Quintero Noda et al. 2016). The synthetic spectra were calculated for a wavelength grid of 113 data points in 0.025 Å steps, four times denser than the CRISP data set. Stratification of the atmospheric parameters obtained by the inversions is given as a function of the logarithm of the optical depth scale at 500 nm (hereafter $\log\tau$). The response function of the Ca II 8542 Å line is expanded to $\log\tau \sim 0$ and $-5.5$ (see Quintero Noda et al. 2016 for details). As our Ca II 8542 Å line scan is $-1.5$ Å to $+1.2$ Å from line core, the analysis of the response functions shows that it provides diagnostics in the layers between $\log\tau \sim -1$ and $-5.5$ (see Figure 6 in Quintero Noda et al. 2016).

To improve convergence, the inversions were performed in three cycles, expanding on the suggestion of Ruiz Cobo & del Toro Iniesta (1992) and as implemented in de la Cruz Rodríguez et al. (2012). In the first cycle and for the first scan, the inversions were performed with four nodes in temperature and one in LOS velocity, with the initial guess model being the FAL-C atmosphere (Fontenla et al. 1993). The convergence of the models obtained from the first cycle was improved by applying horizontal interpolation to recompute the inverted parameters of the pixels with a low quality of fits. A second cycle was then performed with an increased number of nodes (seven for temperature and four for LOS velocity) and the interpolated initial guess model constructed from the first cycle. The synthetic profiles obtained from the second cycle tend to have deeper absorptions than the observations, even for the quiet Sun. The comparison between the solar atlas profile of the Fourier transform spectrometer (FTS) disk center (Neckel 1999), convolved with a model of the CRISP transmission profile with FWHM = 107.3 mÅ provided by de la Cruz Rodríguez et al. (2015b), and the average SST/CRISP flat-field disk-center profile does not show an adequate coincidence of resulting profiles. This indicates a broader or more asymmetric instrumental profile than the respective model used in NICOLE (the synthetic profiles are convolved with the instrumental profile before comparison with the observations and before the final output). Therefore, in the third cycle we convolved the instrumental profile with a Gaussian of FWHM = 141 mÅ and performed an inversion with the same number of nodes and an initial guess model constructed from the second cycle. This led to a better match between the observed and synthetic spectra. Table 1 summarizes the number of nodes and initial temperature models used in the three cycles. We also convolved the atlas profile with an asymmetric Lorentzian model of the transmission profile for the CRISP transmission profile with FWHM = 0.080 Å. This also provides the required similarity between the atlas and the observed flat-field profiles, suggesting that indeed the transmission profile could be asymmetric. We ran the inversions with the asymmetric Lorentzian profile and the resulting atmospheres were the same as obtained with the CRISP instrumental profile convolved with a symmetric Gaussian with FWHM = 141 mÅ.

**Table 1**
Number of Nodes and Input Atmosphere Models Used during Each Cycle of the Inversion

| Physical Parameter | Cycle 1 | Cycle 2 | Cycle 3 |
|---|---|---|---|
| Temperature | 4 nodes | 7 nodes | 7 nodes |
| LOS velocity | 1 node | 5 nodes | 5 nodes |
| Microturbulence | 1 node | 1 node | 1 node |
| Macroturbulence | none | none | none |
| Input atmosphere | FAL-C | model from Cycle 1 | model from Cycle 2 |

Our observations do not include full Stokes imaging spectroscopic data, so we run NICOLE only for Stokes $I$ profiles. Therefore, in both cycles, the magnetic field vector and the weights for other Stokes parameters were set to zero. We inverted an area of 200 × 200 pixel$^2$ (8.2 × 8.2 Mm$^2$) covering the flare ribbons as well as some non-flaring regions (see left panels of Figure 1). Although our time series comprises 346 spectral scans, we choose only the best scans in terms of spatial resolution. This limits the total number of scans to 35, with a cadence of approximately 1 minute in the time interval 11:38 to 12:09 UT.

## 4. Analysis and Results

Figure 2 presents a Ca II 8542 Å line core image of the region selected for inversions (marked with the orange box in Figure 1). The NICOLE output showing the temperature and the LOS velocity maps is also presented. Temperature and velocity maps are integrated and averaged between $\log\tau \approx -3.5$ and $-5.5$, corresponding to middle and upper chromospheric layers, respectively. The top row shows the images close to the flare peak (∼11:38 UT) and the bottom row shows images 7 minutes later. A temperature map of the inverted region close to flare peak shows temperature enhancements for the two flare ribbons. The LOS velocity map of the same region in the top right panel of Figure 2 reveals downflows at the flare ribbons, while the temperature map in the bottom middle panel indicates that the size of the flare ribbons and the heated areas has decreased dramatically 7 minutes later.

Figure 3 shows the line profiles and temperature/velocity stratifications of three pixels indicated as FL, FF, and QS in Figure 2, with the pixels in different parts of the region under investigation. The best-fit synthetic profiles obtained from the inversion at 11:38:20 UT are also shown. There are basically three different shapes of line profile over the selected region during the flare: absorption, emission, and those with central reversal. In the non-flaring areas (QS), Ca II 8542 Å shows the well-known absorption line profile. The line profiles of the flaring loops (FLs) connecting the flare footpoints (FFs) (ribbons) have central reversals, whereas profiles of the FF are in full emission without a central reversal. Figure 3 shows that the observed spectra are generally reproduced by the synthetic best-fit spectra. The QS temperature is close to the

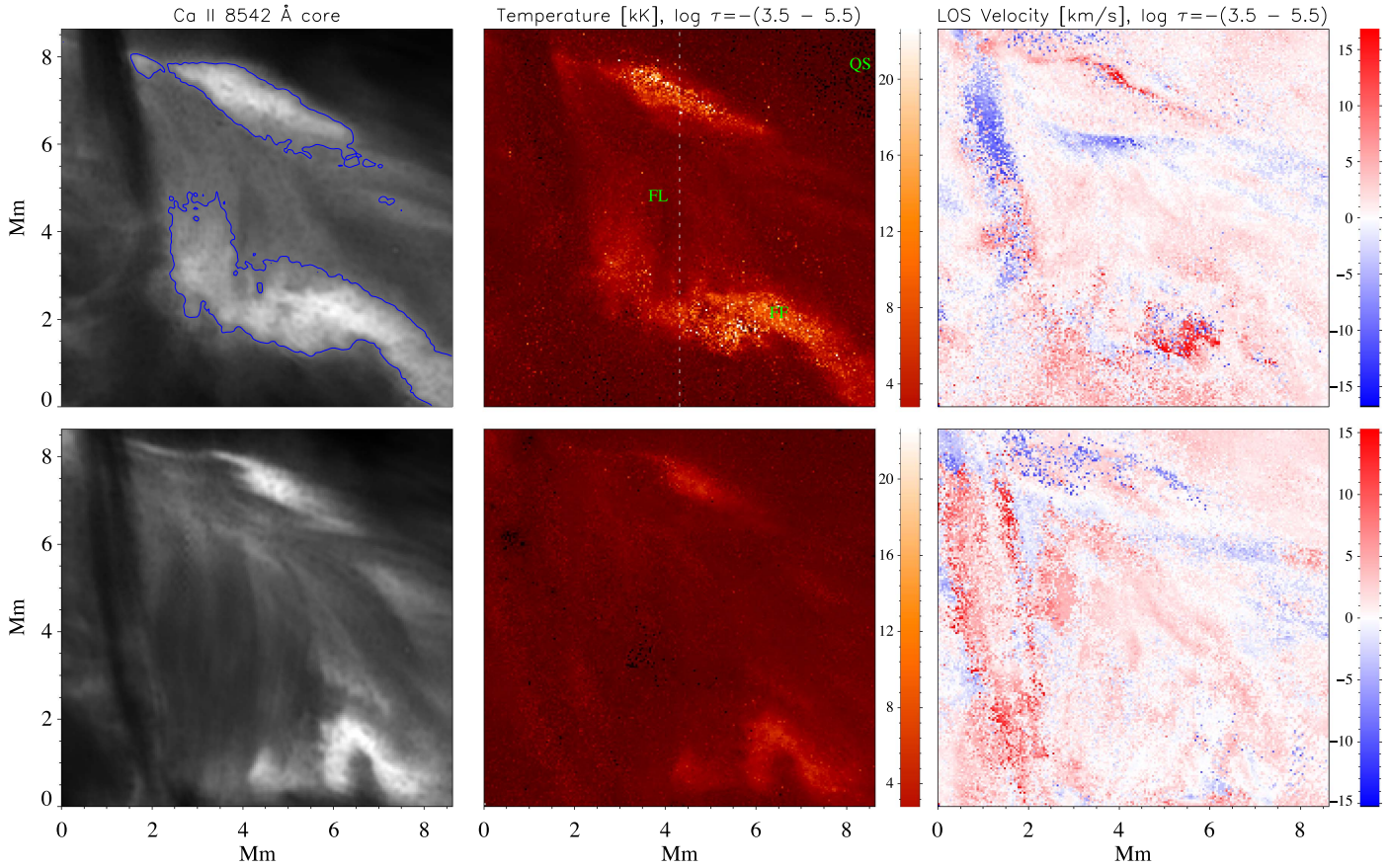


**Figure 2.** The top row shows the images at 11:38 UT (4 minutes after the flare peak) and the bottom row images at 11:45 UT. SST images of the flaring region in the Ca II 8542 Å line core are shown in the left panels. NICOLE outputs showing the temperature and the LOS velocity maps in the interval between log $\tau \sim -3.5$ and $-5.5$ are provided in the middle and right panels, respectively. Blue contours show the area analyzed in this paper, which has intensity levels greater than 30% of the intensity maximum. "FL," "FF," and "QS" mark the selected pixels at the flare loop, flare footpoint, and quiet Sun, respectively, and are discussed in the text in more detail. The red and blue colors in the dopplerograms represent positive Doppler velocities (downflows) and negative Doppler velocities (upflows), respectively. The white dotted line indicates the location where a vertical cut of the atmosphere is made for detailed analyses.

FAL-C temperature profile, whereas the FL has a higher chromospheric temperature at log $\tau \sim -2.5$ and $-5.5$ (middle panels of Figure 3), with the FF showing the highest temperatures.

In Figure 4 we present the temporal evolution of the temperature and velocity stratifications for the flaring and non-flaring pixels. The temperature of the footpoints is enhanced across the chromosphere between optical depths of log $\tau \sim -2.5$ and $-5.5$. As time progresses, the temperature in the lower chromosphere between log $\tau \sim -2.5$ and $-3.5$ decreases gradually from $T \sim 5$–6.5 kK to $T \sim 5$ kK. In the middle and upper chromosphere, between log $\tau \sim -3.5$ and $-5.5$, the temperature decreases from $T \sim 6.5$–20 kK to $T \sim 5$–10 kK during about 15 minutes (top left panel of Figure 4). The velocity field for the flaring pixel is dominated by weak upflows that decrease gradually with time, while the temperature and velocity of the non-flaring areas are lower and unchanged in the chromosphere at log $\tau \sim -1$ and $-5.5$ (right panels of Figure 4).

In Figure 5 we show the evolution of the temperature stratifications using density maps that have been produced with the superimposition of individual pixels from the flaring region marked with blue contours in Figure 2. It must be noted that the stratifications of the pixels with a low quality of fit, such as unphysically low or high temperature plateaus or dips and peaks, were ignored and are not included in the density plots. Our density maps confirm that the most intensively heated layers are in the middle and upper chromosphere at optical depths of log $\tau \sim -3.5$ and $-5.5$, reaching temperatures between ~6.5 and 20 kK. The temperature stratification of the layers below log $\tau \sim -2.5$ remains unchanged during the flare and is consistent with the QS FAL-C model used as the initial atmosphere for the inversions (Figure 5). In the top left panel of Figure 6 we show a vertical cut of the net temperature enhancement of the flare close to its peak (~11:38 UT), where an average temperature stratification obtained from quiet, non-flaring areas has been subtracted. The two bright regions at ~2 and 7.5 Mm show the temperature enhancements of the flare ribbons.

As noted in Section 3, NICOLE calculates the basic thermodynamic parameters that define the internal energy of the system, such as the density and electron pressure, using the equation of state, temperature stratification, and upper boundary condition under the assumption of hydrostatic equilibrium. To estimate the energy content of the flaring chromosphere, we compute the internal energy $e$ using the relationship

$$e = \frac{1}{\gamma - 1}\frac{p}{\rho}, \quad (1)$$

where $p$ and $\rho$ are the gas pressure and density, respectively, and $\gamma = 5/3$ is the ratio of specific heats (Aschwanden 2004;

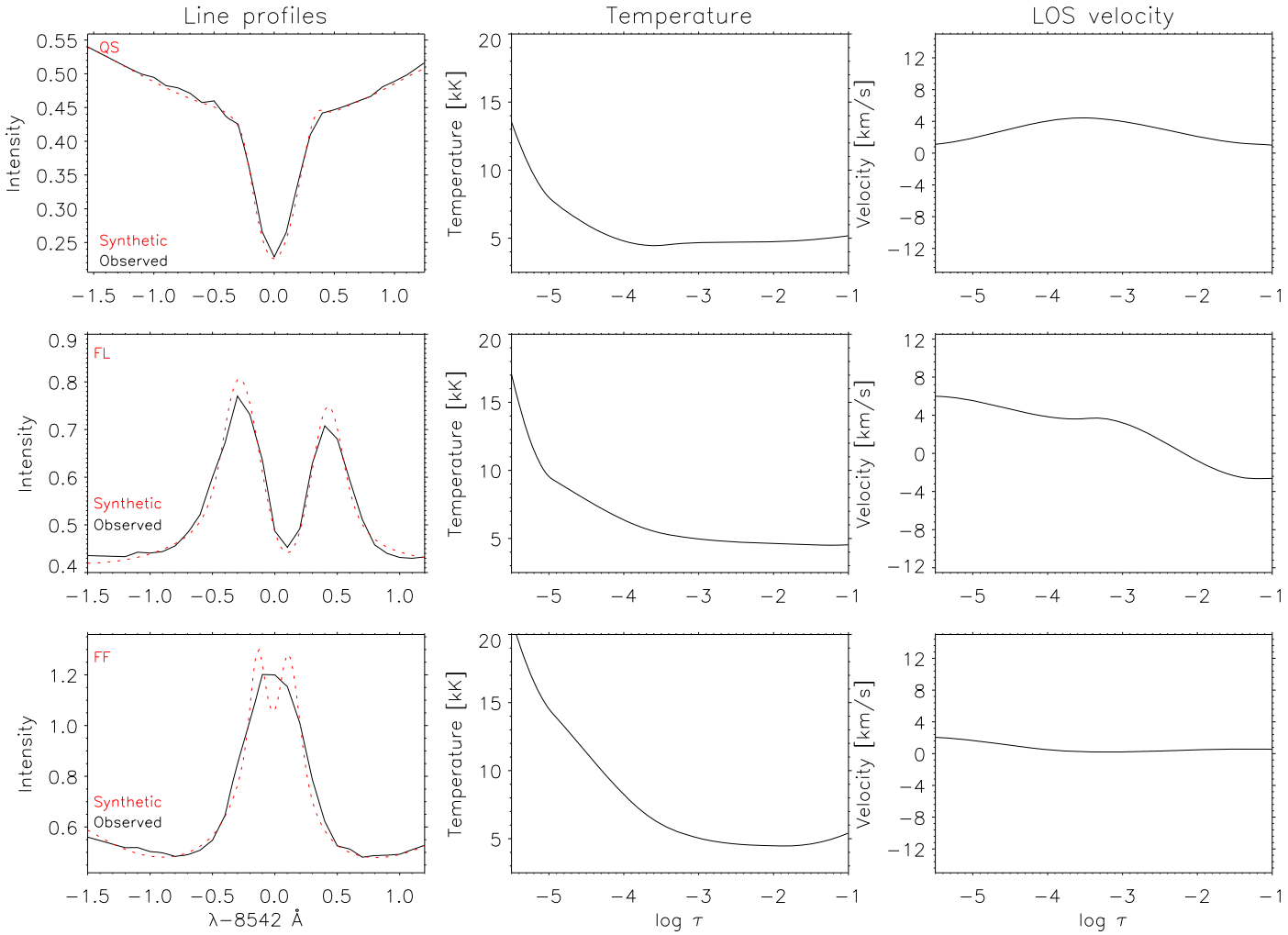


**Figure 3.** Observed (black) and best-fit synthetic (red dotted) Ca II 8542 Å line profiles together with temperature and velocity stratifications for the three selected pixels indicated as FL, FF, and QS in Figure 2.

Beck et al. 2013). The top right panel of Figure 6 shows a vertical cut of the excess energy density per unit mass close to flare maximum at 11:38 UT, which is the internal energy, $e(x, y, \tau)$, computed for each pixel minus an average internal energy, $e_q(x, y, \tau)$, estimated from quiet, non-flaring areas. A three-dimensional (3D) rendering of this excess energy density for an inner part of the inverted data cube is also shown in the bottom left panel of Figure 6. It illustrates that the enhancement in energy density coincides with the locations of flare ribbons where the temperature enhancements are detected. The ratio of total internal energy of this part of the inverted surface ($S \approx 5.3 \times 6.7$ Mm$^2$) to the internal energy for an equally sized surface of the QS as a function of optical depth is presented in the bottom middle panel of Figure 6. This shows that the energy of the flaring region is increased in the range of optical depths log $\tau$ from $\sim -2.5$ to –5.5 compared to the internal energy of the QS. The ratio has a peak at log $\tau \approx -5$ where the internal energy of the inverted flare region is increased by a factor of close to three over the QS. As time progresses, the ratio decreases gradually to $\sim$1 after about 15 minutes, meaning that the atmosphere (energetically speaking) has reached QS levels. The total energy of the chromospheric volume shown in the bottom left panel of Figure 6 (integrated over the range of optical depth log $\tau$ from $\approx$–3.5 to –5.5) is estimated to be $\sim 10^{24}$ erg close to the flare peak, decreasing linearly to a QS energy level of $\sim 6 \times 10^{23}$ erg after approximately 15 minutes (bottom right panel of Figure 6). We note that, due to the high viewing angle of the observed region, the vertical extent of the model atmospheres shown and described in Figure 6 does not correspond to the true geometrical height of the lower solar atmosphere. NICOLE derives the geometrical height from the optical depth scale and the temperature plus density/pressure stratifications, and an optical depth $\tau$ refers to layers at different geometrical heights in different models. Therefore, a temperature/energy excess derived through the models does not show accurately the energy distribution as a function of geometrical height, but it does so as a function of optical depth.

## 5. Discussion and Conclusions

We have presented spectroscopic observations of the Ca II 8542 Å line in a C8.4-class flare. The line profiles of the flare ribbons are in total emission without a central reversal, whereas those of FLs, which connect the FFs, show central reversals

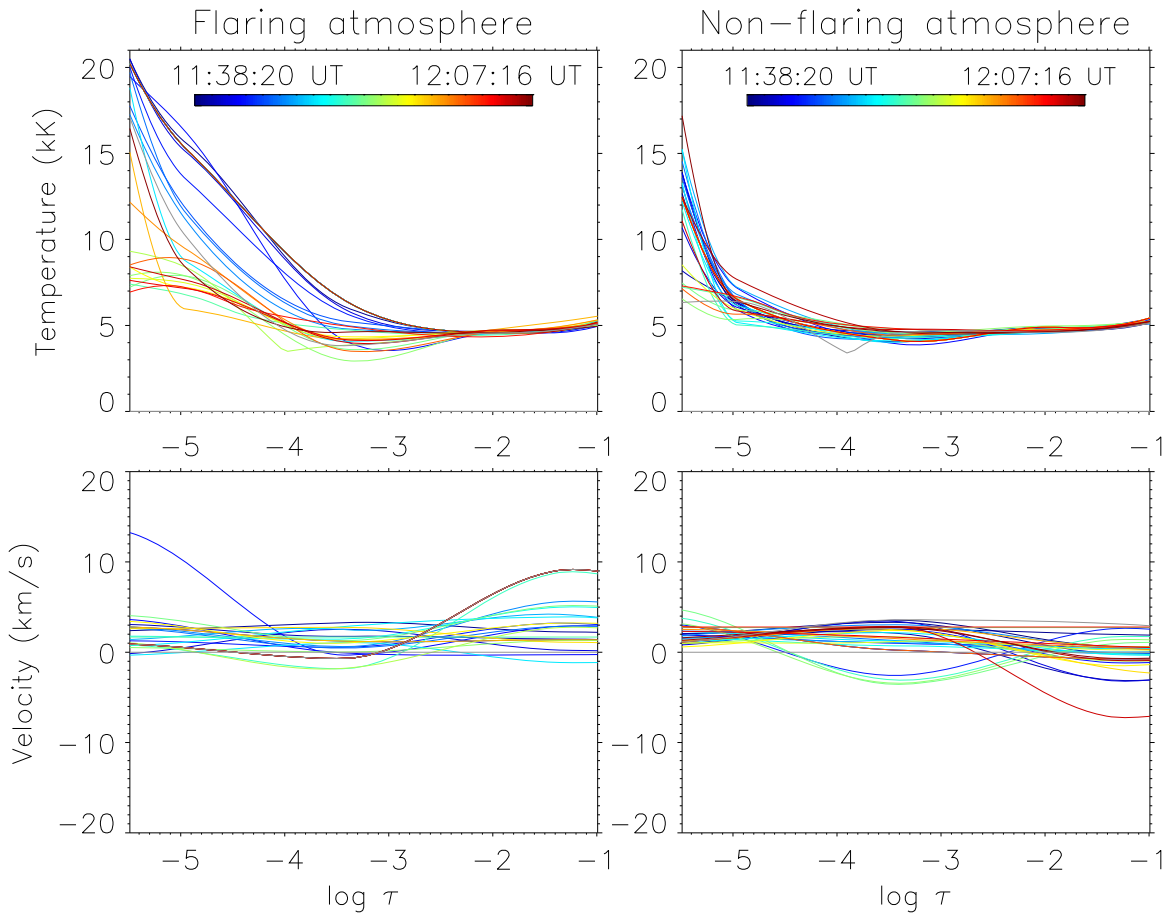


**Figure 4.** The temporal evolution of the temperature and velocity stratifications for the flaring and non-flaring pixels marked with QS and FF in Figure 2, respectively.

(Figure 3). In the quiet Sun the line is in absorption (Figure 3). The analysis of synthetic chromospheric spectral line profiles produced with radiative hydrodynamic models has shown that the changes in temperature, radiation field, and population density of the energy states make the line profile revert from absorption into emission with or without a central reversal (Kuridze et al. 2015, 2016). In a recent investigation, Kuridze et al. (2016) studied the flare profiles of the Na I D1 line, which also forms in the optically thick chromosphere. The heating of the lower solar atmosphere by the nonthermal electron beam makes the Na I D1 line profiles go into full emission. However, when the beam heating stops, the profiles develop a central reversal at the line cores. Unfortunately, as there is no energy flux from electrons in NICOLE, that cannot be used to investigate how the emission and centrally reversed profiles of the Ca II 8542 Å line are formed. However, the analysis of the synthetic line profiles from the RADYN simulations shows that for a strong electron beam heating (model F11) the Ca II 8542 Å line profiles are in full emission but develop a central reversal after beam heating in the relaxation phase of the simulation (Kuridze et al. 2015). For a weak flare run (model F9), the synthesized Ca II 8542 Å profile exhibits a shallow reversal during the beam heating phase that deepens during the relaxation phase.

The comparison of synthetic line profiles and their temperature stratifications from different models obtained from the inversions presented here indicates that the depth of the central reversal depends on the temperature at the core formation height ($\sim -5.5 < \log\tau < -3.5$), i.e., a higher temperature produces a shallower central reversal (Figure 3). This could explain why flare ribbons, which are believed to be the primary site of nonthermal energy deposition and intense heating, have profiles in full emission, whereas FLs, which are secondary products of the flare and hence less heated areas, have central reversals.

We constructed semi-empirical models of the flaring atmosphere using the spectral inversion NLTE code NICOLE to investigate its structure and evolution. Models were generated at 35 different times during the flare, starting at 4 minutes after the peak. The construction of the models is based on a comparison between observed and synthetic spectra. Close to the line core, where the self-reversal is formed, we find a small discrepancy between the synthetic and observed spectra of the flare ribbons (Figure 3). The synthetic profiles have a small absorption in the core, in contrast to the observed profiles, which are in full emission (bottom left panel of Figure 3). This influences the narrow layer of core formation height and hence does not have a strong effect on the overall output model. A possible reason for the observed discrepancy could be the lower degree of ionization of Ca II in the flaring atmosphere compared to the ionization used in NICOLE (Wittmann 1974). Furthermore, the models constructed close to the flare peak are characterized by a high quality of fit and provide a better match with the observed spectra. This is because, as time from flare maximum progresses, the well-defined shapes of emission and centrally reversed line profiles become flatter and feature more irregular shapes, which causes

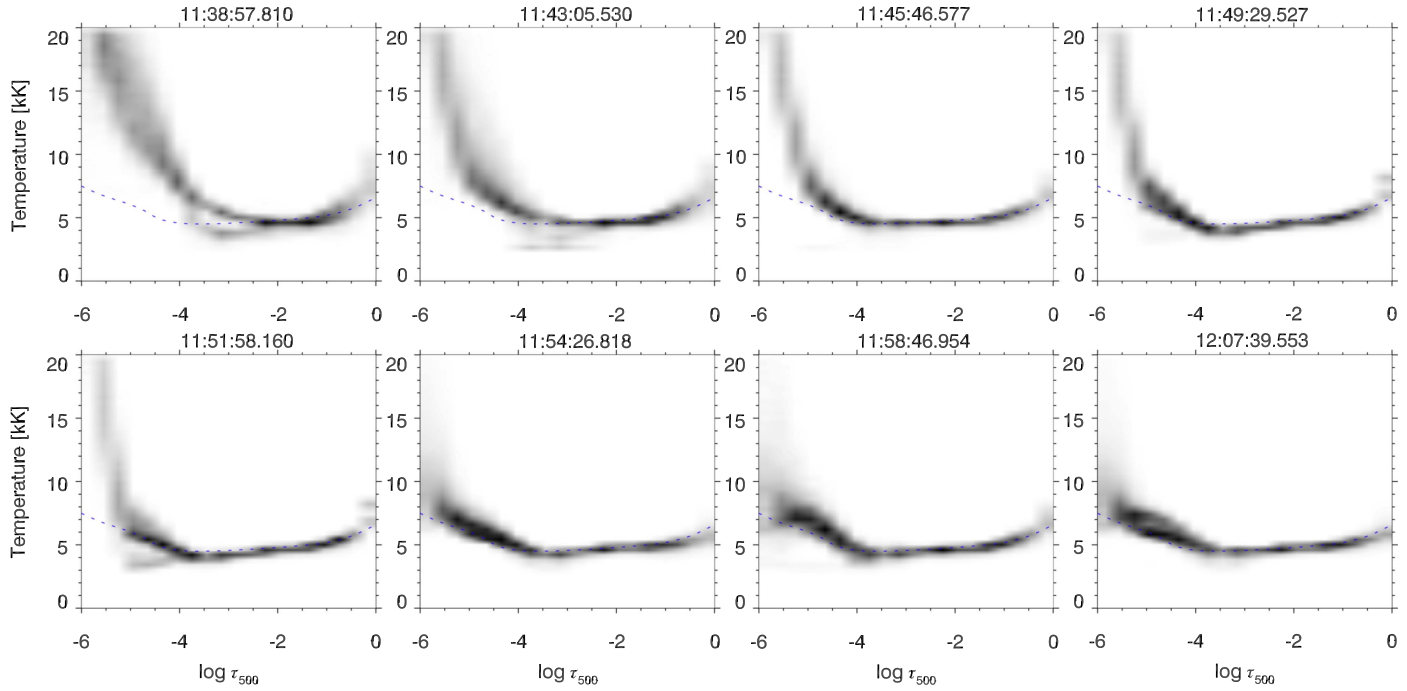


**Figure 5.** Density maps showing the evolution of the temperature stratification during the flare. Each map is produced by superimposing the stratification of around 2000 individual models, selected for quality of fit at each time. The selected region is marked with blue contours in Figure 2. The blue dashed line depicts the FAL-C model, used as the initial atmosphere for the inversions.

NICOLE to encounter difficulties in finding atmospheres that reliably fit such profiles.

Our analysis of the constructed model shows that the most intensively heated layers in the flaring lower atmosphere are the middle and upper chromosphere at optical depths of $\log\tau\sim-3.5$ and $-5.5$, respectively, with temperatures between $\sim$6.5 and 20 kK. The temperatures of these layers decrease to typical QS values ($\sim$5–10 kK) after about 15 minutes (Figure 5). In the photosphere, below $\log\tau\approx-2.5$, there is no significant difference in temperature stratifications between quiescence and flaring (Figure 5). This agrees with some of the previous results (e.g., Falchi & Mauas 2002), which show that during the flare the atmosphere is unchanged below $\sim$600 km. However, it must be noted that, because the observations presented in this work started 4 minutes after the flare peak, it is possible that the temperature in the deeper layers of the atmosphere was affected during the impulsive phase.

The velocity field indicates that the observed field of view is dominated by weak downflows at optical depths of $\log\tau\sim-1$ and $-5.5$ associated with the post-flare chromospheric condensations (Figures 2 and 3). Centrally reversed Ca II 8542 Å profiles show excess emission in the blue wing (blue asymmetry) with a redshifted line center (left middle panel of Figure 3). Similar to blue asymmetries observed in H$\alpha$, Na I D1, and Mg II flaring line profiles (Abbett & Hawley 1999; Kuridze et al. 2015, 2016; Kerr et al. 2016), the asymmetry found in Ca II 8542 Å seems to be related to the velocity gradients associated with the chromospheric condensations. The core of the Ca II 8542 Å profile presented in the left middle panel of Figure 3 is redshifted owing to the downflows at the height of core formation (right middle panel of Figure 3). Velocity decreases downward toward the wing formation regions, producing a positive velocity gradient with respect to the height inward. This gradient can modify the optical depth of the atmosphere in such a way that higher-lying (core) atoms absorb photons with longer wavelengths (red wing photons), and the blue asymmetry in the centrally reversed peak is formed. We note that semi-empirical models of the flaring atmosphere above sunspots (Berlicki et al. 2008) indicate that at the early phase of the flare the flaring layers (loops) are dominated by chromospheric upflows (evaporations) rather than downflows as detected in our study. This difference may be due to the difference in phases of the flares as we detect the downflows in the late phase (4 minutes after the flare peak).

Using the stratification of gas density and pressure obtained from NICOLE, under the assumption of hydrostatic equilibrium, we investigated the evolution of the total internal energy of the lower solar atmosphere covering the formation height of Ca II 8542 Å. Our analysis shows that the total energy of the chromosphere close to the flare maximum ($\sim$11:38 UT) is significantly increased in the range of optical depth $\log\tau$ from $\sim-3.5$ to $-5.5$ compared to the internal energy of the QS (Figure 6). A maximum enhancement was detected at $\log\tau\approx-5$, where the total internal energy, integrated over a selected area of the flare, is a factor of three greater than the integral over the same area of a QS region. This internal energy reduces to the relaxed, QS state after approximately 15 minutes. The total energy of the inverted box shown in the left panel of Figure 6 is estimated to be $\sim10^{24}$ erg close to the flare peak, and to decrease linearly to the QS energy level of $\sim6\times10^{23}$ erg after 15 minutes (bottom right panel of Figure 6). We note that hydrostatic equilibrium may not be a valid assumption for accurate estimations of the thermodynamic parameters, and hence for the energy for a highly dynamical process such as a solar flare. However, we emphasize that modern inversion algorithms currently use the assumption of hydrostatic equilibrium only to obtain pressures and density stratifications, and we believe that quantities such as the evolution of the energy ratio with time should be unaffected by this approximation.

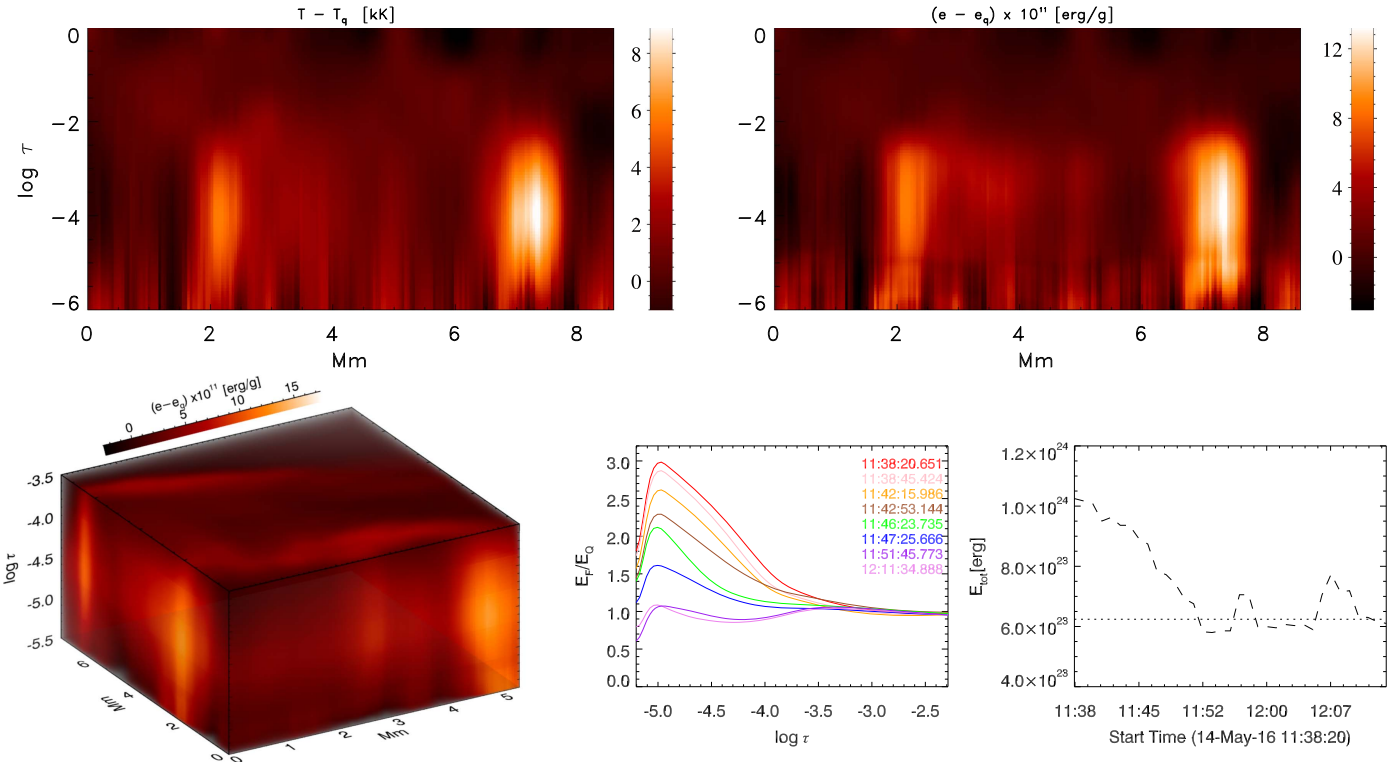


**Figure 6.** Top left: vertical cut of the temperature stratification with the quiet, non-flaring temperature subtracted. The maps are produced from the locations indicated by the white dotted line in Figure 2. Top right: vertical cut of the excess energy density per unit mass, which is the internal energy $e(x, y, \tau)$ computed for each pixel minus an average internal energy $e_q(x, y, \tau)$ estimated from quiet, non-flaring areas. Bottom left: 3D rendering of the excess energy density produced for an inner part (only $S \approx 5.3 \times 6.7$ Mm$^2$) of the inverted data cube. The maps have been smoothed over 10 pixels (∼400 km) along the $x$-axis. Bottom middle: evolution of the ratio of the area-integrated internal energy for the inverted region shown in the bottom left panel over an equally sized area of QS. Bottom right: evolution of the total energy (dashed line) integrated over an inverted region presented in the bottom left panel. The total energy of the same-size QS volume is overplotted as a dotted line.

To our knowledge, we have presented the first spectroscopic inversions, in NLTE, of the solar chromospheric line (Ca II 8542 Å) to produce semi-empirical models of the flaring atmosphere. The temperature stratification obtained from the inversion is in good agreement with other semi-empirical NLTE flare models constructed without inversion codes, and with atmospheres obtained with forward modeling using radiative hydrodynamic simulations (Machado et al. 1980; Falchi & Mauas 2002; Allred et al. 2005; Kuridze et al. 2015; Rubio da Costa et al. 2016). This suggests that NLTE inversions can be reliably applied to the flaring chromosphere.

The research leading to these results has received funding from the European Community's Seventh Framework Programme (FP7/20072013) under grant agreement No. 606862 (F-CHROMA). The Swedish 1 m Solar Telescope is operated on the island of La Palma by the Institute for Solar Physics (ISP) of Stockholm University at the Spanish Observatorio del Roque de los Muchachos of the Instituto de Astrofísica de Canarias. The SST observations were taken within the Transnational Access and Service Programme: High Resolution Solar Physics Network (EU-7FP 312495 SOLARNET). This research has made use of NASA's Astrophysics Data System. This project made use of the Darwin Supercomputer of the University of Cambridge High Performance Computing Service (http://www.hpc.cam.ac.uk/), provided by Dell Inc. using Strategic Research Infrastructure Funding from the Higher Education Funding Council for England and funding from the Science and Technology Facilities Council. The authors benefited from the excellent technical support of the SST staff, in particular from the SST astronomer Pit Sütterlin. This work was supported by the Science Grant Agency project VEGA 2/0004/16 (Slovakia) and by the Slovak Research and Development Agency under the contract No. SK-AT-2015-0022. This article was created by the realization of the project ITMS No. 26220120029, based on the supporting operational research and development program financed from the European Regional Development Fund. A.H. thank the Austrian FWF (project P 27765) for support. The work of T.V.Z. was supported by the Austrian Fonds zur Förderung der wissenschaftlichen Forschung (FWF) project P 28764-N27 and by the Shota Rustaveli National Science Foundation project DI-2016-17 and by the Austrian Scientific-technology collaboration (WTZ) project SK 12/2016.

## ORCID iDs

D. Kuridze https://orcid.org/0000-0003-2760-2311
V. Henriques https://orcid.org/0000-0002-4024-7732
M. Mathioudakis https://orcid.org/0000-0002-7725-6296
J. Koza https://orcid.org/0000-0002-7444-7046
T. V. Zaqarashvili https://orcid.org/0000-0001-5015-5762
J. Rybák https://orcid.org/0000-0003-3128-8396
F. P. Keenan https://orcid.org/0000-0001-5435-1170

## References

Abbett, W. P., & Hawley, S. L. 1999, ApJ, 521, 906
Allred, J. C., Hawley, S. L., Abbett, W. P., & Carlsson, M. 2005, ApJ, 630, 573
Aschwanden, M. J. 2004, Physics of the Solar Corona. An Introduction (Chichester, UK: Praxis Publishing)

Asensio Ramos, A., Trujillo Bueno, J., & Landi Degl'Innocenti, E. 2008, ApJ, 683, 542
Beck, C., Choudhary, D. P., Rezaei, R., & Louis, R. E. 2015, ApJ, 798, 100
Beck, C., Rezaei, R., & Puschmann, K. G. 2013, A&A, 553, A73
Berlicki, A., Heinzel, P., Schmieder, B., & Li, H. 2008, A&A, 490, 315
Berlicki, A., Heinzel, P., Schmieder, B., Mein, P., & Mein, N. 2005, A&A, 430, 679
Carlsson, M., & Stein, R. F. 1997, ApJ, 481, 500
Cauzzi, G., Reardon, K. P., Uitenbroek, H., et al. 2008, A&A, 480, 515
de la Cruz Rodríguez, J., Hansteen, V., Bellot-Rubio, L., & Ortiz, A. 2015a, ApJ, 810, 145
de la Cruz Rodríguez, J., Löfdahl, M. G., Sütterlin, P., Hillberg, T., & Rouppe van der Voort, L. 2015b, A&A, 573, A40
de la Cruz Rodríguez, J., Rouppe van der Voort, L., Socas-Navarro, H., & van Noort, M. 2013, A&A, 556, A115
de la Cruz Rodríguez, J., Socas-Navarro, H., Carlsson, M., & Leenaarts, J. 2012, A&A, 543, A34
de la Cruz Rodríguez, J., & van Noort, M. 2016, SSRv, in press
Falchi, A., & Mauas, P. J. D. 2002, A&A, 387, 678
Fletcher, L., Dennis, B. R., Hudson, H. S., et al. 2011, SSRv, 159, 19
Fontenla, J. M., Avrett, E., Thuillier, G., & Harder, J. 2006, ApJ, 639, 441
Fontenla, J. M., Avrett, E. H., & Loeser, R. 1990, ApJ, 355, 700
Fontenla, J. M., Avrett, E. H., & Loeser, R. 1991, ApJ, 377, 712
Fontenla, J. M., Avrett, E. H., & Loeser, R. 1993, ApJ, 406, 319
Fontenla, J. M., Curdt, W., Haberreiter, M., Harder, J., & Tian, H. 2009, ApJ, 707, 482
Gan, W.-Q., & Fang, C. 1987, SoPh, 107, 311
Gan, W. Q., & Mauas, P. J. D. 1994, ApJ, 430, 891
Gan, W. Q., Rieger, E., & Fang, C. 1993, ApJ, 416, 886
Gingerich, O., Noyes, R. W., Kalkofen, W., & Cuny, Y. 1971, SoPh, 18, 347
Henriques, V. M. J. 2012, A&A, 548, A114
Henriques, V. M. J. 2013, PhD thesis, Univ. Stockholm
Kerr, G. S., Fletcher, L., Russell, A. J. B., & Allred, J. C. 2016, ApJ, 827, 101
Kuridze, D., Mathioudakis, M., Christian, D. J., et al. 2016, ApJ, 832, 147
Kuridze, D., Mathioudakis, M., Simões, P. J. A., et al. 2015, ApJ, 813, 125
Lagg, A., Ishikawa, R., Merenda, L., et al. 2009, in ASP Conf. Ser. 415, The Second Hinode Science Meeting: Beyond Discovery-Toward Understanding, ed. B. Lites et al. (San Francisco, CA: ASP), 327
Leenaarts, J., Carlsson, M., Hansteen, V., & Rouppe van der Voort, L. 2009, ApJL, 694, L128
Machado, M. E., Avrett, E. H., Vernazza, J. E., & Noyes, R. W. 1980, ApJ, 242, 336
Machado, M. E., & Linsky, J. L. 1975, SoPh, 42, 395
Mauas, P. 2007, in ASP Conf. Ser. 368, The Physics of Chromospheric Plasmas, ed. P. Heinzel, I. Dorotovič, & R. J. Rutten (San Francisco, CA: ASP), 203
Mauas, P. J. D. 1990, ApJS, 74, 609
Mauas, P. J. D. 1993, ApJ, 414, 928
Mauas, P. J. D., Machado, M. E., & Avrett, E. H. 1990, ApJ, 360, 715
Neckel, H. 1999, SoPh, 184, 421
Pietarila, A., Socas-Navarro, H., & Bogdan, T. 2007, ApJ, 663, 1386
Quintero Noda, C., Shimizu, T., de la Cruz Rodríguez, J., et al. 2016, MNRAS, 459, 3363
Rubio da Costa, F., Kleint, L., Petrosian, V., Liu, W., & Allred, J. C. 2016, ApJ, 827, 38
Ruiz Cobo, B., & del Toro Iniesta, J. C. 1992, ApJ, 398, 375
Rutten, R. J., & Uitenbroek, H. 2012, A&A, 540, A86
Scharmer, G. B. 2006, A&A, 447, 1111
Scharmer, G. B., Bjelksjo, K., Korhonen, T. K., Lindberg, B., & Petterson, B. 2003a, Proc. SPIE, 4853, 341
Scharmer, G. B., Dettori, P. M., Lofdahl, M. G., & Shand, M. 2003b, Proc. SPIE, 4853, 370
Scharmer, G. B., Narayan, G., Hillberg, T., et al. 2008, ApJL, 689, L69
Socas-Navarro, H., de la Cruz Rodríguez, J., Asensio Ramos, A., Trujillo Bueno, J., & Ruiz Cobo, B. 2015, A&A, 577, A7
Socas-Navarro, H., & Trujillo Bueno, J. 1997, ApJ, 490, 383
Socas-Navarro, H., Trujillo Bueno, J., & Ruiz Cobo, B. 2000, ApJ, 530, 977
Uitenbroek, H. 1989, A&A, 213, 360
van Noort, M., Rouppe van der Voort, L., & Löfdahl, M. G. 2005, SoPh, 228, 191
Vernazza, J. E., Avrett, E. H., & Loeser, R. 1981, ApJS, 45, 635
Vissers, G., & Rouppe van der Voort, L. 2012, ApJ, 750, 22
Wedemeyer-Böhm, S., & Carlsson, M. 2011, A&A, 528, A1
Wittmann, A. 1974, SoPh, 35, 11